GOLD Mission's Observation about the Geomagnetic Storm Effects on the Nighttime Equatorial Ionization Anomaly (EIA) and Equatorial Plasma Bubbles (EPB) During a Solar Minimum Equinox

Deepak Kumar Karan[1], Richard W Eastes[2], Robert Edward Daniell[3], Carlos Martinis[4], and William E. McClintock[2]

[1]Laboratory for Atmospheric and Space Physics, University of Colorado
[2]Laboratory for Atmospheric and Space Physics
[3]Ionospheric Physics Consulting
[4]Boston University

December 7, 2022

Abstract

The nighttime ionospheric response to a geomagnetic storm occurred on 23-29 September 2020 is investigated over the South American, Atlantic, and West African longitude sectors using NASA's Global-scale Observations of the Limb and Disk (GOLD) measurements. On 27 September the solar wind conditions were favorable for prompt penetration electric fields (PPEF) to influence the equatorial ionosphere over extended longitudes. The equatorial ionization anomaly (EIA) crests were shifted 8º-10º poleward compared to the quiet time monthly mean across ˜65º- 35ºW during the main phase. Ionosonde hmF2 (peak electron density height) measurements from Fortaleza (GG: -3.9ºN and -38.4ºW) indicated a stronger prereversal enhancement this evening than other nights. As a result, Equatorial Plasma Bubbles (EPB) occurred at these longitudes on this evening. This is the first simultaneous investigation of EIA morphology and EPB occurrence rate over an extended longitude range from geostationary orbit during a geomagnetic storm.

1

GOLD Mission's Observation about the Geomagnetic Storm Effects on the Nighttime Equatorial Ionization Anomaly (EIA) and Equatorial Plasma Bubbles (EPB) During a Solar Minimum Equinox

Deepak Kumar Karan[1], Richard W. Eastes[1], Robert E. Daniell[2], Carlos R. Martinis[3], and William E. McClintock[1]

[1]Laboratory for Atmospheric and Space Physics, University of Colorado, Boulder, CO, USA
[2]Ionospheric Physics, Stoughton, MA, USA
[3]Center for Space Physics, Boston University, MA, USA

Corresponding author: Deepak Kumar Karan (Deepak.Karan@lasp.colorado.edu)

Key Points:

- First simultaneous observations of geomagnetic storm effects on EIA morphology and EPB occurrence rate from the geostationary orbit

- Maximum poleward shift of the EIA crests and increase in EPB occurrence rate is observed during storm's main phase on 27 September 2020

- Concurrent increase of hmF2 from digisonde observation confirms the strengthening of the plasma fountain effect during postsunset hours

Abstract

The nighttime ionospheric response to a geomagnetic storm occurred on 23-29 September 2020 is investigated over the South American, Atlantic, and West African longitude sectors using NASA's Global-scale Observations of the Limb and Disk (GOLD) measurements. On 27 September the solar wind conditions were favorable for prompt penetration electric fields (PPEF) to influence the equatorial ionosphere over extended longitudes. The equatorial ionization anomaly (EIA) crests were shifted 8°-10° poleward compared to the quiet time monthly mean across ~65°- 35^oW during the main phase. Ionosonde hmF2 (peak electron density height) measurements from Fortaleza (GG: -3.9^{o}N and -38.4^{o}W) indicated a stronger prereversal enhancement this evening than other nights. As a result, Equatorial Plasma Bubbles (EPB) occurred at these longitudes on this evening. This is the first simultaneous investigation of EIA morphology and EPB occurrence rate over an extended longitude range from geostationary orbit during a geomagnetic storm.

Plain Language Summary

The effects of a geomagnetic storm that occurred during 23-29 September 2020 on the nighttime equatorial ionospheric behavior is investigated using NASA's Global-scale Observations of the Limb and Disk (GOLD) measurements. On each evening EIA crests locations and brightnesses and EPB occurrence rates are obtained over the South American, Atlantic, and West African longitude sectors. On 27 September the solar wind conditions were favorable for the penetration of interplanetary electric fields to the equatorial ionosphere over the dusk longitude sectors (~ 35^oW Lon). The PPEF strengthened the pre-reversal enhancement (PRE) and thereby enhanced the plasma fountain effect. Ionospheric F2 layer height increase is confirmed by digisonde measurements at Fortaleza (GG: 3.9^{o}S and 38.4^{o}W). On this day maximum poleward shifts compared to the quiet time monthly mean values are observed across ~65°- 35° W longitude during the storm's main phase. EPBs occurrence rate was maximum on this night. The present study reports the first simultaneous investigation of EIA morphology (crests locations and brightnesses) and EPB occurrence rates over an extended longitude range during a geomagnetic storm from a geostationary orbit.

2

1 Introduction

The Equatorial Ionization Anomaly (EIA) (also known as the Appleton Anomaly) is a persistent ionospheric feature at equatorial and low latitudes (Appleton, 1946). The equatorial F region eastward electric fields ($\vec{E}$) and horizontal northward magnetic fields ($\vec{B}$) create a vertical, upward ($\vec{E} X \vec{B}$) drift over the magnetic equator. Due to this vertical drift, the ionospheric plasma moves to higher altitudes and diffuses along the magnetic field lines to low latitudes. The overall effect is known as the fountain effect (Martyn, 1955; Hanson and Moffet, 1966). The plasma density shows a minimum at the magnetic equator and two maxima around 15o-20o north and south of it. This creates a double-peaked structure in the latitudinal distribution of the F region plasma with crests on each side and a trough over the magnetic equator, which is called the EIA.

During geomagnetic disturbances, several storm-induced electric fields (e.g., prompt penetration electric field (PPEF), disturbance dynamo electric fields (DDEF)) contribute to the ionospheric electric fields over the equatorial and low latitude regions. During southward conditions of interplanetary magnetic field (IMF) Bz, effects of the Y-component (dawn-dusk) of interplanetary electric field (IEF) can reach equatorial and low latitudes. The changes in the equatorial ionospheric electric fields due to the storm time magnetosphere-ionosphere coupling are well understood (Chakrabarty et al., 2008, 2015; Fejer et al., 2008; Rout et al., 2019, and references therein). The resultant electric field can increase or decrease the vertical drift and thereby, can change the strength of the plasma fountain effect and EIA crests locations.

The response of the EIA crests to geomagnetic disturbances using measurements (Abdu et al, 1991; Pallamraju et al., 2004; Mannucci et al., 2005; Astafyeva, 2009; Aa et al., 2019; Balan et al., 2018; Karan et al., 2018; Akala et al., 2021) and simulations (Huba et al., 2005; Tsurutani et al., 2008; Lu et al., 2013) have been reported in the literature. Most of these papers discuss the impact of extreme geomagnetic storms on the daytime EIA crests altitudes and electron densities. There are few studies on the effect of geomagnetic disturbance electric fields on the post sunset/nighttime behavior of EIA crests (Abdu et al, 1991; Huba et al., 2005; Balan et al., 2018; Rout et al., 2019). Most of them investigated the storm time EIA behavior over a narrow longitude range.

Geomagnetic storms not only affect the EIA morphology but also affect the behavior of ionospheric plasma irregularities. Due to the pre-reversal enhancement (PRE) at the magnetic equator, local times shortly after sunset favor the development of ionospheric plasma irregularities.

90 Lower atmospheric waves seed the perturbation for the generation of such irregularities (Aa et al.,

91 2020). The irregularities manifest as equatorial plasma bubbles (EPBs) in ionospheric images.

92 Electric field perturbations during geomagnetic active periods are reported to enhance (Tulasi Ram

93 et al., 2008; Basu et al., 2010; Kil et al., 2016; Patra et al., 2016; Zakharenkova and Cherniak,

94 2020; Cherniak and Zakharenkova, 2022) and sometimes inhibit (Aarons et al., 1991; Abdu et al.,

95 1995; Spogli et al., 2016) the irregularities. Using the AE-parameterized Fejer-Scherliess model

96 for disturbance vertical drifts versus storm time and local time, Martinis et al., (2005) were able to

97 summarize these apparently contradictory effects.

98   In the present study, we have used NASA's Global-scale Observations of the Limb and

99 Disk (GOLD) instrument data to investigate the effects of a CIR-storm occurred during 23-29

100 September 2020 on both the postsunset EIA crests locations and brightnesses, and EPB occurrence

101 rates over the South American, Atlantic, and West African longitude sectors. To the best of our

102 knowledge, this study is the first simultaneous investigation on geomagnetic storm effects on EIA

103 morphology and EPB occurrence rate over an extended longitude range from geostationary orbit.

104 Geomagnetic storms of varying strengths can damage the ground and space-based infrastructures

105 and also injurious to human health, engineering, and applications (Pulkkinen et al., 2017). With

106 this regard the present investigation on the effects of a moderate CIR geomagnetic storm

107 simultaneously on the nighttime EIA morphology and EPB occurrence rate will assist space

108 weather community's understanding to develop future forecasting capabilities.

109

110 **2 Data**

111 GOLD images are the primary data set in this work. The imager was launched on 25 January 2018

112 and is located in geostationary orbit at 47.5^{o} W. The imager has two identical, independent

113 channels (channel A and B; CHA and CHB hereafter), each has a scan mirror and interchangeable

114 slits. GOLD has the advantage of observing the American, Atlantic, and West African longitudinal

115 regions. This provides a unique opportunity to unambiguously observe the spatial-temporal

116 evolution of various ionospheric-thermospheric features of the Earth during post-sunset periods.

117 The GOLD instrument, observation modes, and data products are discussed in Eastes et al., (2017,

118 2019, 2020) and McClintock et al., (2020). GOLD makes disk and limb observations, and

119 occultations of the Earth at FUV emission wavelength (~132-162 nm). Only the nighttime partial

120 disk, 135.6 nm images of the Earth are considered in the present study. The nighttime peak

121 emission altitude for OI 135.6 nm is assumed to be 300 km when geolocating the pixels. Nightside

122 partial disk observations use both channels. The observations start at 20:10 UT using CHB only,

123 alternating between northern and southern hemispheres. An image is obtained every 15 minutes,

124 initially over the African sector, and follows the sunset terminator towards the South American

125 sector. From 23:10 UT both channels make simultaneous observations over the northern and

126 southern hemispheres at nearly the same longitude regions. The observation sequence is explained

127 in detail by Karan et al., 2020.

128   Solar wind parameters (magnetic field, electric field, plasma flow speed, proton density,

129 plasma temperature, and flow pressure), and geomagnetic indices (SYM-H and ap index) are used

130 to understand the solar wind conditions and different phases of the geomagnetic storm and to

131 evaluate storm's effect on equatorial ionosphere model ionospheric electric fields (Manoj and

132 Maus, 2012) are used. F2 layer height responds to changes in the electric field. So, variations of

133 ionospheric F2 layer height (hmF2), are obtained from ionosonde observations at Fortaleza (GG:

134 3.9° S and 38.4° W).

135

136 **3 Results and Discussions**

137 Figures 1a-1c show the hourly averaged solar wind parameters observed at the L1 point from 21

138 September 2020 (DOY=265) to 4 October 2020 (DOY=278). Figure 1(d) shows the SYM-H and

139 ap indexes derived from ground-based magnetometer measurements. Figure 1(e) shows modeled

140 ionospheric PPEF. The horizontal blue dashed lines in Figure 1(e) indicate the times when GOLD

141 takes nighttime observations (20:10 to 00:45 UT). The fluctuating solar wind temperature, plasma

142 flow pressure, SYM-H, and ap index show the onset of a CIR driven geomagnetic storm (Borovsky

143 and Denton, 2006) on DOY 267 (23 September). During this period at three instances (DOY 268

144 – 07 UT and 269 – 22 UT, shown by vertical dotted lines, and DOY 271 – 20 UT, shown by

145 vertical dashed line) the polarity and magnitude of IMF Bz and IEF Ey were suitable to make the

146 solar wind geoeffective. SYM-H and ap variations (in Figure 1d) clearly show the main phases of

147 the storm at these three times. On DOY 271 (27 September) at 20 UT the sunset terminator was

148 over ~ 35° W GG longitude. At this time the IMF Bz and IEF Ey reached maxima of -5.6 nT and

149 3.19 mV/m, respectively. The solar wind speed and proton density sharply increased to 600 km/s

150 and 10 cc-1, respectively and the plasma temperature and flow pressure increased to 3.5×10^5 K

151 and 5 nPa, respectively. Such sharp increases in the solar wind parameters contribute to a steep

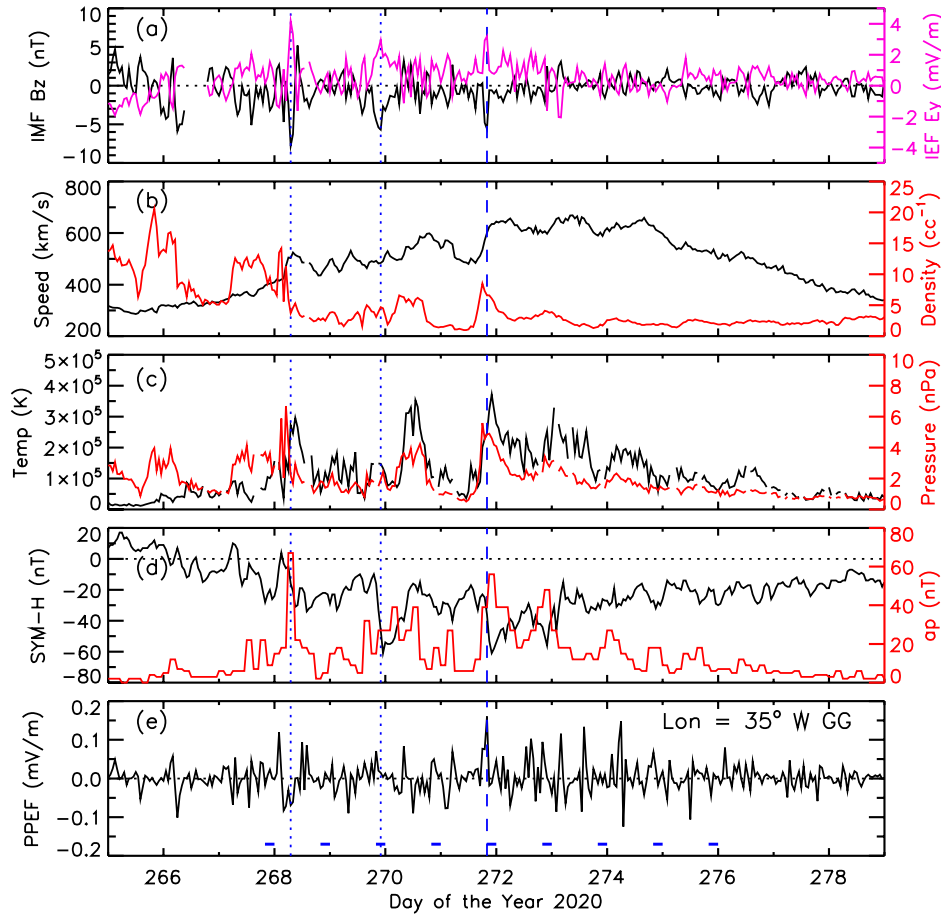*Figure 1shows the (a) IMF Bz and IEF Ey, (b) plasma flow speed and proton density, (c) plasma temperature and flow pressure, (d) SYM-H and ap, and (e) model PPEF during 21 September 2020 (DOY=265) to 5 October 2020 (DOY=279).*

152   main phase of the storm which is confirmed through the SYM-H and ap indices (Figure 1d). The

153   SYM-H and ap reached a maximum of –60 nT and 60 nT, respectively. At this time the model

154   PPEF over 35o W GG longitude (longitude of sunset terminator) is eastward but small, 0.16 mV/m

155   (Figure 1e). This model PPEF is not sufficient to create a strong vertical drift. However, the near

156   simultaneous increase in IEF Ey (Figure 1a) and the direction of the model PPEF may indicate a

157   storm's positive impact on the equatorial ionosphere over sunset longitude regions. On DOY 268,

158   the timing (~07 UT) of the storm coincided with GOLD's day disk observations. On DOY 269 the

159   main phase of the storm occurred ~ 22 UT when the sunset terminator was over West South

160   America which is covered in a single GOLD image. Further, the solar wind parameters and PPEF

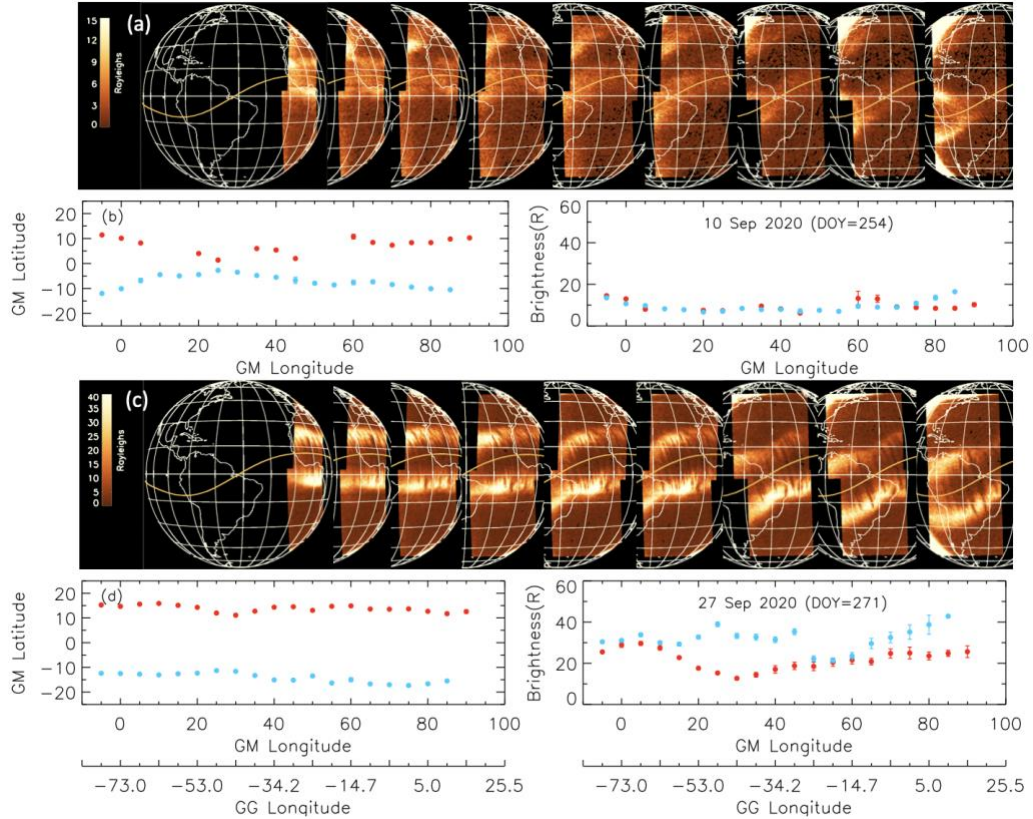161   did not show any significant enhancements during this time.

162

Figure 2(a) shows the nighttime 135.6 nm images of the Earth taken by GOLD imager on 10 September 2020, a geomagnetic quiet day (max ap =4); (b) (left) shows the North (red dots) and South (blue dots) EIA crests obtained from all images shown in (a); (b) (right) shows the 135.6 nm brightness at the EIA crests with corresponding colors as in (b) left. Figure 2(c) and (d) are similar to figure 2(a) and (b) but for 27 September 2020, a geomagnetic disturbed day (max ap = 56).

Figure 2(a) (left to right) shows the composite nightside partial disk images taken by GOLD on DOY 254 (10 September 20:10 to 00:45 UT), a geomagnetic quiet day. As time progresses, the sunset terminator moves westward. So, the longitude coverage of each scan increases (from 23º over West Africa to ~40º over South America). These images are re-mapped into quasi dipole geomagnetic co-ordinates (Laundal and Richmond, 2017) using the International Geomagnetic Reference Field scalar potentials (Thébault et al., 2015). From the remapped images, variations in 135.6 nm brightness with respect to (w.r.t.) magnetic latitudes are obtained at an interval of 1º magnetic longitude. Maxima in the latitudinal variation of the brightness give the location of EIA crests. Following this method, EIA crests latitudes and brightnesses are obtained from all the images. Sometimes low brightnesses create extraneous EIA crests locations which are filtered out in the analysis which is explained in detail by Eastes et al., (2021). From the filtered

174   values, the average and standard deviation of the North (N) and South (S) crests latitudes and

175   brightnesses are obtained every 5° longitude bin. Figure 2(b) shows the EIA crests latitudes (left)

176   and brightnesses (right) (N- red and S- blue) with their standard deviations obtained from the

177   images shown in Figure 2(a). The EIA crests locations at 45º-55º magnetic longitudes were not

178   computed due to low signal levels. In Figure 2(a) brightnesses increase at the northern mid latitudes

179   (~ 30º N) can be seen. An ongoing investigation on this feature is in progress and will be

180   communicated separately. Figures 2 (c,d) are similar to Figures 2(a,b) but for DOY 271 (27

181   September), a geomagnetic active day. On this day the EIA crests are further from the magnetic
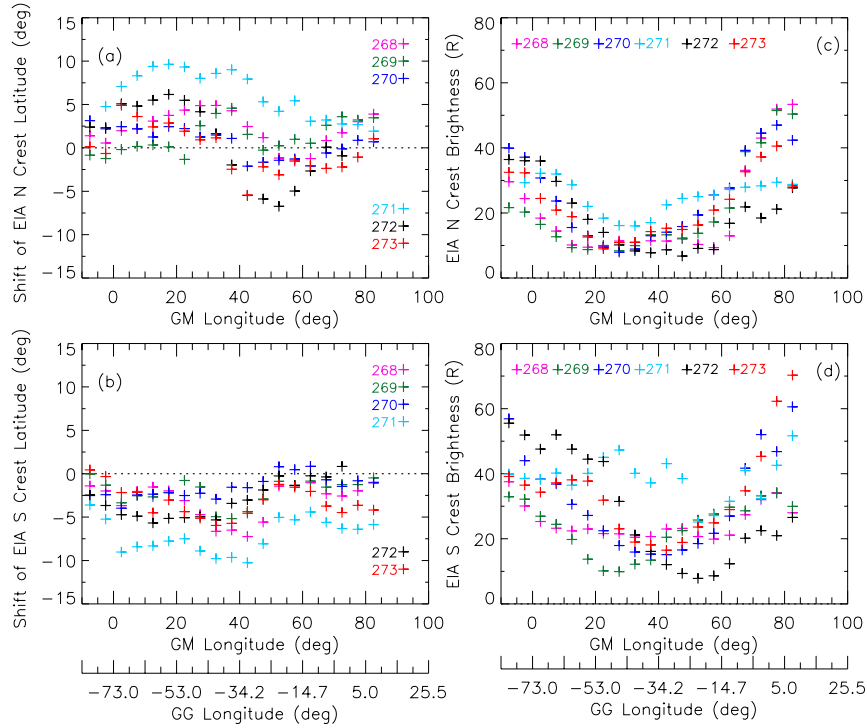
182   equator and are brighter.

Figure 3 shows the shift of EIA North (a) and South (b) crests on the disturbed days (DOY 268 to 273) compared to the geomagnetic quiet days mean value for September 2020. (c) and (d) show the 135.6 nm brightnesses at the North and South EIA crests on the disturbed days.

183

184   Following the procedure mentioned in the previous paragraph, monthly mean EIA crests

185   latitudes and brightnesses are computed for September 2020, considering quiet days (with ap

186   values less than 20 nT). The relative shifts in EIA crests latitudes compared to monthly mean

187   values are calculated for the storm days (DOY 268-273). Figures 3(a,b) show the N and S EIA

188 crests poleward shifts on the storm days. The longitudinal variations of the shifts show similar
189 patterns on these days. This might be indicating a similar systematic longitudinal variation of the
190 electric fields on these days. Figures 3(c and d) show the brightness of the N and S EIA crests. On
191 these days, in general, the EIA crests brightnesses are higher over West African and South
192 American longitude sectors than the Atlantic longitudes. On DOY 271 the shifts of both crests
193 were consistently greater than the other nights. A maximum shift of ~8°-10° is observed over ~ 10°
194 - 40° GM Lon (~65°- 35° W GG Lon). Both EIA crests over this longitude sector are brighter on
195 DOY 271. Over ~35° W GG longitude, the S EIA crest is brighter than the N EIA crest by ~ 20 R.
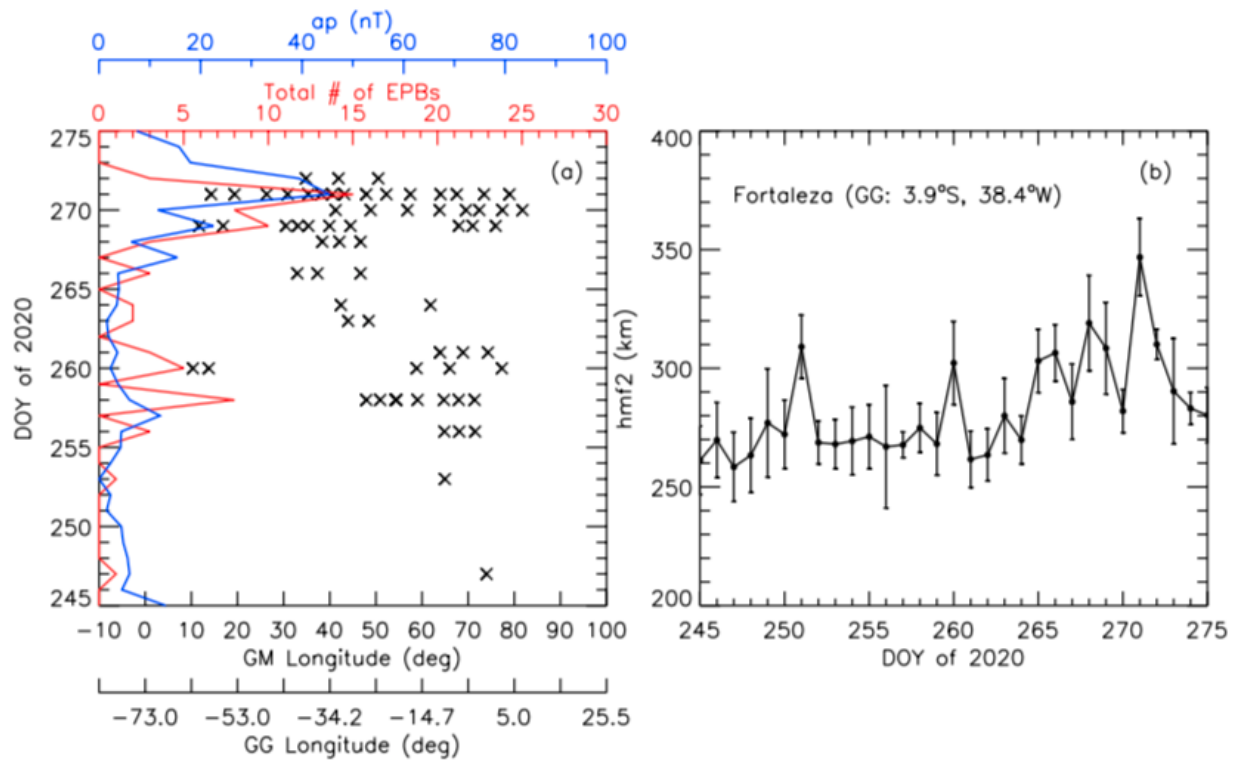196

Figure 4(a) shows EPB longitudes (cross symbol) obtained from nighttime images taken by GOLD imager during September 2020. Day-to-day variations of total EPBs observed (red line) and ap index (blue line) are shown. (b) shows the hmF2 variation during September 2020 obtained from ionosonde at Fortaleza (GG: 3.9° S and 38.4° W), a geomagnetic equatorial station.

197 In order to study the effects of this geomagnetic storm on the behavior of ionospheric
198 plasma irregularities, we investigated EPB occurrences for the full month. An automated tool
199 (described in Karan et al., 2020) is used to obtain the EPBs longitudes from all the images taken
200 on each night. Figure 4(a) shows all the EPBs observed by GOLD from 1 September to 7 October

201 2020 as a function of longitude. On the first 11 days (DOY 245 to 255) the EPBs occurrence was

202 rare, but later it increases during the storm days. Towards the end of September and the beginning

203 of October (DOY 273 to 280), geomagnetic activity was quiet and EPBs occurrence was low. The

204 red line shows the total number of EPBs and the blue line shows the daily mean ap index during

205 18 to 00 UT (period close to GOLD observations). It can be seen that EPBs occurrence rate and

206 geomagnetic activity mostly agree with each other. Most EPBs were observed east of ~ 35º W GG

207 longitude during the quiet days (DOY 245 to 268). On DOY 269 and DOY 271 (geomagnetically

208 active) EPBs are observed west of 35º W GG longitude where EIA crests poleward shifts were

209 maxima. The possible cause for the EIA crests poleward shift and EPBs occurrence rate increase

210 could be the strengthening of the equatorial electric field due to PPEF effects. If this is true, then

211 the equatorial F2 layer might have moved to a higher altitude. Ionosonde data from Fortaleza (GG:

212 -3.9º N and -38.4º W) are used to investigate the behavior of hmF2, the height of peak electron

213 density (Reinisch and Galkin, 2011). This station was chosen because it is located near the

214 magnetic equator and at a longitude where the maximum EIA shift is observed. The mean and

215 standard deviation of hmF2 values during 18 to 24 UT for the entire month of September 2020 are

216 shown in Figure 4(b). This time interval includes the pre and post sunset hmF2 information. On

217 DOY 271, hmF2 was maximum (~350 km) among all the days.

218   This maximum hmF2 on DOY 271 can be explained by the time (20 UT) of peak IEF Ey

219 (Figure 1a) and variation of SYM-H index (Figure 1d). To examine the enhancement of the ring

220 current, the rate of decrease of SYM-H (i.e. dSYM-H/dt) is investigated (not shown here). dSYM-

221 H/dt has a maximum negative excursion of -12 nT/30 min at 20 UT. The simultaneity of peak IEF

222 Ey and the sharp decrease in SYM-H at 20 UT suggests that there was a prompt penetration of

223 eastward electric fields into the equatorial and low latitudes around local dusk sectors (~ 35º W

224 GG longitudes). This eastward PPEF increased the normal prereversal enhancement thereby lifting

225 the ionospheric layer up as observed in hmF2 (Figure 4b) and shifting the EIA crests (Figures

226 3a,b). EIA crests locations shift was maximum over ~ 10º - 40º GM Lon (~65º- 35º W GG Lon).

227 These longitudes were in the local sunset hours during the main phase of the storm and thus, were

228 influenced by the PPEF. Tulasi Ram et al, 2008 and Basu et al., 2010 have reported the prompt

229 penetration of eastward electric fields into low and equatorial latitudes where the local time

230 corresponds to post sunset hours during the entire main phase of the storm. Their findings match

231 our observations. The shift decreased west of ~65º W GG longitude where local sunset occurred

232 after the main phase. Also, the shifts were less east of ~35º W GG longitude. These longitudes
233 were already in the nightside and had passed through the PRE-process before the main phase of
234 the storm. GOLD's observations over a wide longitudinal coverage have brought an important
235 understanding of the storm's longitudinal effect.

236   The lifting of the ionospheric layer to higher altitudes due to strong PRE makes the
237 ionosphere conducive for RT-instability. This situation is favorable for the occurrence and
238 development of ionospheric plasma irregularities (Abdu et el., 2018). In the whole month, the
239 highest number of EPBs are observed on the most geomagnetic active day (DOY 271). An Increase
240 in EPBs occurrence rate over ~ 10º - 40º GM Lon (~65º- 35º W GG Lon) on the geomagnetic
241 active day indicates the storm's positive effect on EPBs occurrence rate.

242 **4 Conclusions**

243 The present study investigates the effects of a CIR driven geomagnetic storm on the nighttime
244 ionosphere over the South American, Atlantic, and West African longitudes. From GOLD images
245 of the 135.6 nm emission, northern and southern EIA crests latitudes are obtained for all days of
246 September 2020, including the September 23-29 CIR storm. The EIA crests latitudes during the
247 storm are compared to those before it. While there were significant shifts in the EIA crests
248 locations throughout the storm, the shifts on one night, 27 September, were greater than the others.
249 On that night a maximum shift of ~8º-10º was observed across ~10º - 40º GM Lon (~65º- 35º W
250 GG Lon) which correspond to local sunsets during the main phase of the storm. An increase in
251 hmF2 confirms the enhancement of PRE-strength due to storm induced PPEF effect. This favors
252 the development of ionospheric plasma irregularities. EPBs occurrence rate was maximum on
253 DOY 271. The present study reports the first simultaneous investigation of EIA morphology
254 (crests locations and brightnesses) and EPB occurrence rate over an extended longitude range
255 during a geomagnetic storm from geostationary orbit.

References

267 Aa, E., Zou, S., Ridley, A. J., Zhang, S.-R., Coster, A. J., Erickson, P. J., et al. (2019). Merging of
268 storm time midlatitude traveling ionospheric disturbances and equatorial plasma bubbles. Space
269 Weather, 17, 285– 298. https://doi.org/10.1029/2018SW002101.

270 Aa, E., Zou, S., Eastes, R., Karan, D. K., Zhang, S.-R., Erickson, P. J., & Coster, A. J. (2020).
271 Coordinated ground-based and space-based observations of equatorial plasma bubbles. Journal of
272 Geophysical Research: Space Physics, 125. e2019JA027569.
273 https://doi.org/10.1029/2019JA027569.

274 Abdu, M. A., Sobral, J. H. A., de Paula, E. R., & Batista, I. S. (1991). Magnetospheric disturbance
275 effects on the Equatorial Ionization Anomaly (EIA)—An overview. Journal of Atmospheric and
276 Terrestrial Physics, 53, 757–771. https://doi.org/10.1016/0021-9169(91)90126-R.

277 Abdu, M. A., I. S. Batista, G. O. Walker, J. H. A. Sobral, N. B. Trivedi, and E. R. de Paula (1995),
278 Equatorial ionospheric fields during magnetospheric disturbances: Local time/longitudinal
279 dependences from recent EITS Campaigns, J. Atmos. Sol. Terr. Phys., 57, 1065– 1083.

280 Abdu, M. A., Nogueira, P. A. B., Santos, A. M., de Souza, J. R., Batista, I. S., & Sobral, J. H. A.
281 (2018). Impact of disturbance electric fields in the evening on prereversal vertical drift and spread
282 F developments in the equatorial ionosphere. Annales Geophysicae, 36(2), 609–620.
283 https://doi.org/10.5194/angeo-36-609-2018.

284 Akala, A. O., Oyedokun, O. J., Amaechi, P. O., Simi, K. G., Ogwala, A., & Arowolo, O. A. (2021).
285 Solar origins of August 26, 2018 geomagnetic storm: Responses of the interplanetary medium and
286 equatorial/low-latitude ionosphere to the storm. Space Weather, 19, e2021SW002734.
287 https://doi.org/10.1029/2021SW002734

288 Astafyeva, E.: Effects of strong IMF Bz southward events on the equatorial and mid-latitude
289 ionosphere, Ann. Geophys., 27, 1175–1187, https://doi.org/10.5194/angeo-27-1175-2009, 2009

290 Appleton, E. (1946). Two Anomalies in the Ionosphere. Nature 157, 691.
291 https://doi.org/10.1038/157691a0

292 Balan N., Liu L. B., and Le H. J. (2018). A brief review of equatorial ionization anomaly and
293 ionospheric irregularities. Earth Planet. Phys., 2(4), 257–275. http://doi.org/10.26464/epp2018025

294 Basu, S., Su. Basu, E. MacKenzie, C. Bridgwood, C. E. Valladares, K. M. Groves, and C. Carrano
295 (2010), Specification of the occurrence of equatorial ionospheric scintillations during the main
296 phase of large magnetic storms within solar cycle 23, Radio Sci., 45, RS5009,
297 doi:10.1029/2009RS004343.

298 Borovsky, J. E., and M. H. Denton (2006), Differences between CME-driven storms and CIR-
299 driven storms, J. Geophys. Res., 111, A07S08, doi:10.1029/2005JA011447.

300 Chakrabarty, D., R. Sekar, J. H. Sastri, and S. Ravindran (2008), Distinctive effects of
301 interplanetary electric field and substorm on nighttime equatorial F layer: A case study, Geophys.
302 Res. Lett.,35, L19108, doi:10.1029/2008GL035415.

303 Chakrabarty, D., D. Rout, R. Sekar,R. Narayanan, G. D. Reeves, T. K. Pant,B. Veenadhari, and K.
304 Shiokawa (2015), Three different types of electric field disturbances affecting equatorial
305 ionosphere during a long-duration prompt penetration event, J. Geophys. Res. Space Physics,120,
306 4993–5008, doi:10.1002/2014JA020759.

307 Cherniak, I., & Zakharenkova, I. (2022). Development of the storm-induced ionospheric
308 irregularities at equatorial and middle latitudes during the 25–26 August 2018 geomagnetic storm.
309 Space Weather, 20, e2021SW002891. https://doi.org/10.1029/2021SW002891

310 Eastes, R.W., McClintock, W.E., Burns, A.G. et al. (2017), The Global-Scale Observations of the
311 Limb and Disk (GOLD) Mission. Space Sci Rev 212, 383–408, doi:10.1007/s11214-017-0392-2.

312 Eastes, R. W., S. C. Solomon, R. E. Daniell, D. N. Anderson, A. G. Burns, S. L. England, C. R.

313 Martinis, and W. E. McClintock (2019), Global-scale observations of the equatorial ionization

314 anomaly. Geophysical Research Letters, 46, 9318–9326, https:// doi.org/10.1029/2019GL084199.

315 Eastes, R. W., McClintock, W. E., Burns, A. G., Anderson, D. N., Andersson, L., Aryal, S., et al.

316 (2020). Initial Observations by the Global-scale Observations of the Limb and Disk (GOLD)

317 mission. Journal of Geophysical Research: Space Physics, 125, e2020JA027823.

318 https://doi.org/10.1029/2020JA027823.

319 Eastes, R. W., D. K. Karan, C. R. Martinis, R. E. Daniell, Q. Gan, A. G. Burns, & W. E.

320 McClintock. (2021) GOLD Observations of Longitudinal Variations in the Nighttime Equatorial

321 Ionization Anomaly (EIA) Crests Latitudes. https://doi.org/10.1002/ essoar.10506272.1.

322 Fejer, B. G., Jensen, J. W., & Su, S.-Y. (2008). Seasonal and longitudinal dependence of equatorial

323 disturbance vertical plasma drifts. Geophysical Research Letters, 35, L20106.

324 https://doi.org/10.1029/2008GL035584.

325 Hanson, W. B., and Moffett, R. J. (1966). Ionization transport effects in the equatorial F region. J.

326 Geophys. Res., 71(23), 5559–5572. https://doi.org/10.1029/JZ071i023p05559

327 Huba, J. D., Joyce, G., Sazykin, S., Wolf, R., and Spiro, R. (2005), Simulation study of penetration

328 electric field effects on the low- to mid-latitude ionosphere, Geophys. Res. Lett., 32, L23101,

329 doi:10.1029/2005GL024162.

330 Karan, D. K. and D. Pallamraju, (2018). Effect of geomagnetic storms on the daytime low-latitude

331 thermospheric wave dynamics, Journal of Atmospheric and Solar-Terrestrial Physics, 170, 35-47,

332 https://doi.org/10.1016/j.jastp.2018.02.003.

333 Karan, D. K., Daniell, R. E., England, S. L., Martinis, C. R., Eastes, R. W., Burns, A. G., &

334 McClintock, W. E. (2020). First zonal drift velocity measurement of equatorial plasma bubbles

335 (EPBs) from a geostationary orbit using GOLD data. J. Geophys. Res. Space Physics, 125,

336 e2020JA028173. https://doi.org/10.1029/2020JA028173

337   Kil, H., W. K. Lee, L. J. Paxton, M. R. Hairston, and G. Jee (2016), Equatorial broad plasma

338   depletions associated with the evening prereversal enhancement and plasma bubbles during the 17

339   March 2015 storm, J. Geophys. Res. Space Physics, 121, 10,209–10,219,

340   doi:10.1002/2016JA023335.

341   Laundal, K. M., and Richmond, A. D. (2017) Magnetic Coordinate Systems, Space Sci Rev, 206,

342   27-59. https://doi.org/10.1007/s11214-016-0275-y

343   Lu, G., J. D. Huba, and C. Valladares (2013), Modeling ionospheric super-fountain effect based

344   on the coupled TIMEGCM-SAMI3, J. Geophys. Res. Space Physics, 118, 2527–2535,

345   doi:10.1002/jgra.50256.

346   Mannucci, A. J., Tsurutani, B. T., Iijima, B. A., Komjathy, A., Saito, A., Gonzalez, W. D., et al.

347   (2005). Dayside global ionospheric response to the major interplanetary events of October 29–30,

348   2003 "Halloween Storms". Geophysical Research Letters, 32, L12S02.

349   https://doi.org/10.1029/2004GL021467

350   Manoj, C., and S. Maus (2012), A real-time forecast service for the ionospheric equatorial zonal

351   electric field, Space Weather,10, S09002, doi:10.1029/2012SW000825

352   Martinis, C. R., M. J. Mendillo, and J. Aarons (2005), Toward a synthesis of equatorial spread F

353   onset and suppression during geomagnetic storms, J. Geophys. Res., 110, A07306,

354   doi:10.1029/2003JA010362.

355   Martyn, D. F. (1955). Theory of height and ionization density changes at the maximum of a

356   Chapman-like region, taking account of ion production, decay, diffusion, and total drift. In

357   Proceedings, Cambridge Conference (pp.254-259). London: Physical Society.

358   McClintock, W. E., Eastes, R. W., Beland, S., Bryant, K. B., Burns, A. G., Correira, J., et al (2020).

359   Global-scale Measurements of the Limb and Disk (GOLD) Mission Implementation:

360   Observations, Data Pipeline and Level 1 Data Products. Journal of Geophysical Research: Space

361   Physics, 125, e2020JA027809. https://doi.org/10.1029/2020JA027809.

362 Pallamraju, D., Chakrabarti, S., and Valladares, C. E. (2004). Magnetic storm-induced
363 enhancement in neutral composition at low latitudes as inferred by O(1D) dayglow measurements
364 from Chile, Ann. Geophys., 22, 3241–3250, https://doi.org/10.5194/angeo-22-3241-2004.

365 Patra, A. K., P. P. Chaitanya, N. Dashora, M. Sivakandan, and A. Taori (2016), Highly localized
366 unique electrodynamics and plasma irregularities linked with the 17 March 2015 severe magnetic
367 storm observed using multitechnique common-volume observations from Gadanki, India, J.
368 Geophys. Res. Space Physics, 121, 11,518–11,527, doi:10.1002/2016JA023384.

369 Pulkkinen, A., Bernabeu, E., Thomson, A., Viljanen, A., Pirjola, R., Boteler, D., et al. (2017).
370 Geomagnetically induced currents: Science, engineering, and applications readiness. Space
371 Weather, 15, 828–856. https://doi.org/10.1002/2016SW001501

372 Reinisch, B. W., and I. A. Galkin, Global ionospheric radio observatory (GIRO), Earth, Planets,
373 and Space, 63, 377-381, doi:10.5047/eps.2011.03.001, 2011.

374 Rout, D., Pandey, K., Chakrabarty, D., Sekar, R., & Lu, X. (2019). Significant electric field
375 perturbations in low latitude ionosphere due to the passage of two consecutive ICMEs during 6–8
376 September 2017. Journal of Geophysical Research: Space Physics, 124, 9494– 9510.
377 https://doi.org/10.1029/2019JA027133.

378 Spogli, L., et al. (2016), Formation of ionospheric irregularities over Southeast Asia during the
379 2015 St. Patrick's Day storm, J. Geophys. Res. Space Physics, 121, 12,211–12,233,
380 doi:10.1002/2016JA023222.

381 Thébault, E., Finlay, C.C., Beggan, C.D., Alken, P., Aubert, J., Barroi, O. et al. (2015).
382 International Geomagnetic Reference Field: the 12th generation. Earth Planet Sp 67, 79,
383 https://doi.org/10.1186/s40623-015-0228-9

384 Tsurutani, B. T., Verkhoglyadova, O. P., Mannucci, A. J., Saito, A., Araki, T., Yumoto, K., et al.
385 (2008). Prompt penetration electric fields (PPEFs) and their ionospheric effects during the great
386 magnetic storm of 30–31 October 2003. Journal of Geophysical Research, 113, A05311.
387 https://doi.org/10.1029/2007JA012879

388   Tulasi Ram, S., P. V. S. Rama Rao, D. S. V. V. D. Prasad, K. Niranjan, S. Gopi Krishna, R.

389   Sridharan, and S. Ravindran (2008), Local time dependent response of postsunset ESF during

390   geomagnetic storms, J. Geophys. Res., 113, A07310, doi:10.1029/2007JA012922

391   Zakharenkova, I., & Cherniak, I. (2020). When plasma streams tie up equatorial plasma

392   irregularities with auroral ones. Space Weather, 18, e2019SW002375.

393   https://doi.org/10.1029/2019SW002375